ADVANCED MATERIALS
www.advmat.de

Multifunctional Terahertz Biodetection Enabled by Resonant Metasurfaces

Ride Wang, Ruan Hao, Dongxiao Li, Lujun Huang, Rundong Jiang, Xiaobao Zhang, Xiao Yang, Lei Wang, Shuming Wang,* Yuri Kivshar,* and Chao Chang**

Testing diverse biomolecules and observing their dynamic interaction in complex biological systems in a label-free manner is critically important for terahertz (THz) absorption spectroscopy. However, traditionally employed micro/nanophotonic techniques suffer from a narrow operating resonance and strong absorption band interference from polar solutions preventing seriously reliable, on-demand biosensor integration. Here, a multifunctional THz plasmonic biosensing platform by leveraging multiple interfering resonances from quasi-bound states in the continuum designed to noninvasively and in situ track the temporal evolution of molecules in multiple analyte systems, is proposed. In contrast to conventional microphotonic sensors, this platform demonstrates substantially broadband performance and reduced footprints, allowing for simultaneous detection of diverse molecular vibrant at multiple spectral points through robust near-field interactions. Furthermore, this sensor enables real-time analysis of amino acid absorption as water evaporates despite its strong overlapping absorption bands in the THz range. By utilizing the real-time format of the reflectance method to acquire a comprehensive spectro-temporal data collection, this approach supports developing a deep neural network to discriminate and predict the composition and proportion of multiple mixtures, obviating the need for frequency scanning or microfluidic devices. This approach offers innovative viewpoints for exploring biological processes and provides valuable tools for biological analysis.

1. Introduction

Optical spectroscopy methodologies, such as infrared (IR) absorption,[1–3] Raman scattering,[4,5] and circular dichroism (CD),[6–8] serve as formidable label-free tools in the detection of biomolecules and the extraction of intricate chemical information in a real-time and noninvasive manner. The terahertz (THz) spectral range is of pivotal importance for these detection approaches since they cover various rotational and collective vibrational frequencies of condensed matter and biomolecules, which enables specific identification of biomolecules with different chemical properties.[9–12] Importantly, all of the basic building blocks of life, such as amino acids, proteins, and nucleic acids, differ in the frequency position, intensity, and shape of their spectra within this spectral range, i.e., exhibit distinct and unique fingerprints. It is worth noting that in a body fluid medium, the oscillation pattern of the molecules to be analyzed will be subjected to many forms of environmental effects, such as van der Waals forces,[13] hydrogen bonding,[14] and so on. For this highly significant and

R. Wang, R. Hao, R. Jiang, X. Zhang, X. Yang, C. Chang
Innovation Laboratory of Terahertz Biophysics
National Innovation Institute of Defense Technology
Beijing 100071, P. R. China
E-mail: wangride@mail.nankai.edu.cn; changc@xjtu.edu.cn

D. Li
Key Laboratory of Optoelectronic Technology & Systems of Ministry of Education
International R & D Center of Micro-nano Systems and New Materials Technology
Chongqing University
Chongqing 400044, China

L. Huang
The Extreme Optoelectromechanics Laboratory (XXL)
School of Physics and Electronic Science
East China Normal University
Shanghai 200241, P. R. China

L. Wang
The Center for Terahertz Waves
School of Precision Instrument and Opto-electronics Engineering
Tianjin University
Tianjin 300072, China

S. Wang
National Laboratory of Solid-State Microstructures
School of Physics
Nanjing University
Nanjing 210093, China
E-mail: wangshuming@nju.edu.cn

The ORCID identification number(s) for the author(s) of this article can be found under https://doi.org/10.1002/adma.202418147

DOI: 10.1002/adma.202418147

widespread phenomenon, using traditional attenuated total reflection (ATR)[15,16] and surface plasmonic resonance (SPR)[17,18] detection techniques is very challenging. It is difficult to analyze the contribution of individual analytes versus separating them from the overall system signal, using sensing effects on net analyte mass and refractive index. Further, for general biological processes in mixed systems that involve multiple elements, distinguishing and monitoring individual components of such heterogeneous mixtures is a central goal of biosensing. Therefore, in order to study the complex interactions of analytes in biological systems, it is crucial to develop new label-free sensing platforms that can independently track absorption fingerprint temporal evolution and distinguish between different biomolecular species.

However, conventional THz detection techniques face some challenges to highly sensitive spectral sensing detection of trace analytes. These challenges include increasing optical absorption by molecular in the specific fingerprint band, miniaturizing device footprints, and reducing the stronger absorption of polar solutions. Broadband-enhanced THz absorption spectroscopy (ETHzAS) emerges as a potential solution to surmount some of these obstacles.[9,19,20] Metasurfaces excel at arbitrarily tailoring the spectral response and light localization in nanophotonic devices and manipulating light on the micro- and nanoscale.[21–27] Engineered metasurfaces can enhance the operating band at will and create intense highly confined hot spots of the electromagnetic field, enabling robust interaction with adjacent analytes and thus making them highly promising candidates for applications in biosensing.[28–31] However, THz metasurface-based biosensors are still far away from satisfaction due to the low-Q resonances. Recently, bound states in the continuum (BICs) have emerged as a powerful tool for achieving high-Q resonances.[32–36] BICs correspond to dark eigenstates that are perfectly decoupled from the exterior environment despite residing in the continuous spectrum. For practical applications, BICs must be transformed into quasi-BICs (QBICs) with finite and high-Q factors.[37,38] Notably, high-Q QBICs are always accompanied by extreme field enhancement, thus holding great promise for enhancing light-matter interactions. There are also some attempts to harness QBICs to improve the performance of biosensors. However, most of the reported QBICs-based sensors are used to detect the refractive index change and only operate in a single narrow band.[39–43] Typically, different biomolecules have a distinct optical response in the THz range. Also, in a real scenario, they are present in the form of a mixture, creating additional challenges to distinguishing them. Thus, it is highly desirable to develop an ultra-compact biosensor that can operate in multi-frequency window so that different biomolecules or multi-components in the mixture can be distinguished in one round test.

2. Results and Discussion

Here, we report a multifunctional THz plasmonic biosensing platform in a label-free manner based on multiple quasi-bound states in the continuums (multi-QBICs) and demonstrate its capability in tracking the intricate dynamics of the absorption fingerprint and enabling concurrent detection of multiple analytes (**Figure 1**). The design comprises arrays of self-similar microantennas introducing discrete asymmetry, which facilitates the simultaneous detection of diverse molecular vibration fingerprints at multiple spectral points. The experimental setup used incident light from backward incidence, which guarantees an enhanced sensing platform that is easy to operate and minimizes the deleterious effects of water absorption on THz signals as it penetrates through the water layer. Our plasmonic reflectance biosensor neatly allows for the in situ real-time resolution of the dynamic process of L-glutamate (L-Glu) absorption fingerprints as the water evaporates. Notably, the collection of subtle real-time signals from the reflectance method allows for the construction of a deep neural network that enables accurate discrimination among simultaneously present biomolecules without the use of any external labels. By combining deep learning techniques with enhanced sensing utilizing the reflectance-enhanced plasmon method, we overcome the challenges associated with experiment complexity and training data availability. This represents a dramatic and transformative advancement for highly sensitive biosensing identification in composite bioanalytical and mixed drug applications, providing new insights into neurotransmitter conduction or throughput processes in fundamental studies.

To perform broad-resonant for molecule-specific detection, we have devised a cutting-edge methodology that integrates elaborate pixelated and multiband plasmonic microantenna arrays (Figure S1, Supporting Information) onto a substrate composed of low-absorption polymethylpentene (TPX). Such compact metasurface-based devices have substantially reduced footprints and broadband performance (Figures S2 and S3, Supporting Information) compared to conventional dielectric-based integrated devices.[35] The incident light comes from the backside of the chip and subsequently reflects to the detector. A notable advantage of the approach lies in its ability to minimize the deleterious effects of water absorption on THz signals. This guarantees accurate sensing of analytes present on the metasurface through the generation of evanescent electric fields emanating from the resonant microantennas. By effectively capitalizing on the potent near-fields generated by metallic micrometer antennas, we can amplify weak vibrational fingerprint signals emitted by nanoscale analytes.

Typically, the resonant frequencies of THz microantenna are spectrally fine-tuned to align with the characteristic vibrational modes of each target biomolecule. Extending the capabilities of this technology to detect multi-fingerprint biosensing necessitates the development of a metasurface supporting multiple resonances and allows us to individually tailor them to match the unique vibrations of different analytes. In doing so, we can precisely read out the molecular absorption features across multiple resonance bands. This exceptional precision not only eradicates

Y. Kivshar
Nonlinear Physics Center
Research School of Physics
Australian National University
Canberra ACT 2601, Australia
E-mail: yuri.kivshar@anu.edu.au
C. Chang
School of Physics
Peking University
Beijing 100871, P. R. China

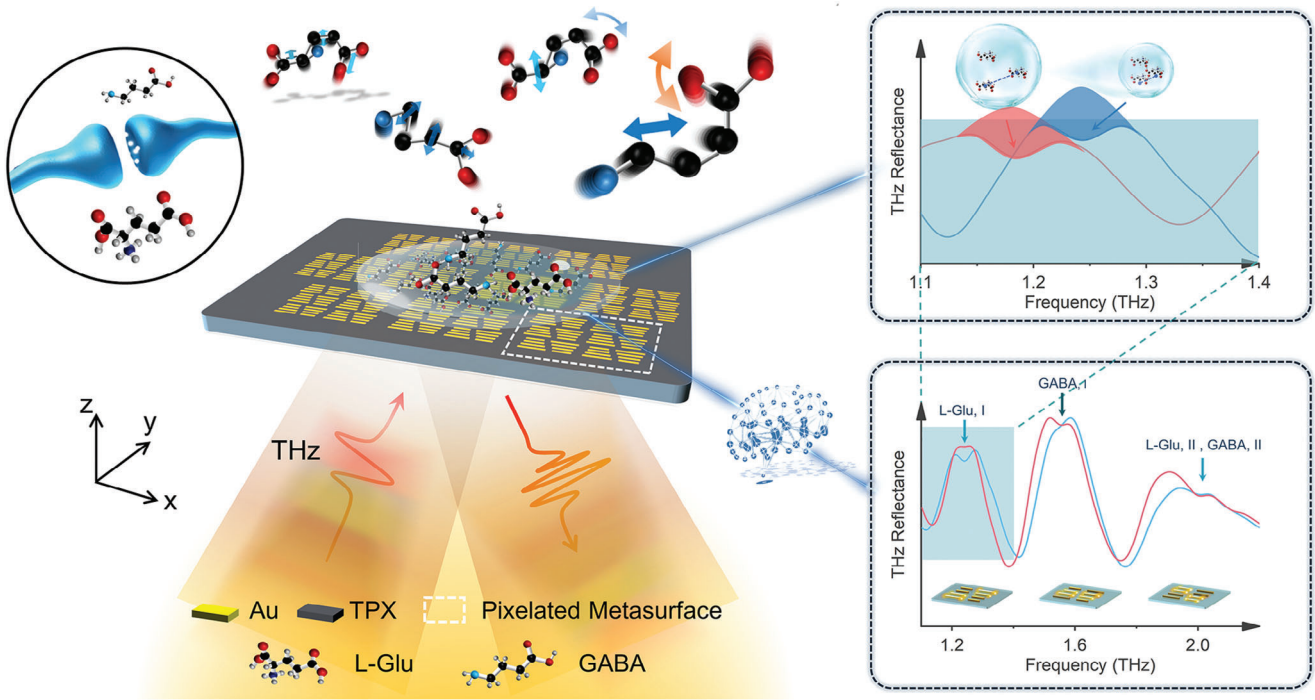

Figure 1. Schematic diagram of a label-free biosensing platform utilizing THz microphotonics technology capable of accurately differentiating components in systems with multiple biological samples. Simultaneous enhancement and detection of changes in analyte absorption spectra are achieved by carefully designing THz multiple microantennas to promote multi-band enhancement to form desired resonance positions. The design enables the excitation of multi-QBICs resonances and perfectly overlaps with the vibrations of the characteristic absorption bands I and II of L-Glu and γ-aminobutyric acid (GABA). The platform works conveniently, allowing for real-time detection of dynamic changes in characteristic fingerprints and substance identification, as well as ratio determination in multi-analyte systems.

false-positive results but also significantly reduces the device's overall footprint.

Current methodologies predominantly employ homogeneous arrays comprised of multiple resonant elements.[44] For the purpose of multiband sensing, however, resonances in such systems typically reduce the excitation efficiency level of higher-order modes associated with smaller resonance feature sizes, leading to a degradation of enhanced THz absorption performance at these resonance frequencies. In addition, electromagnetic coupling between different resonant modes and feature sizes impedes direct spectral tuning. Moreover, the complex structure will increase the design and experimental processing costs. Our method overcomes these three major limitations by designing multiple asymmetric dipole antenna array structures within a single unit cell to assign different resonance frequencies accordingly. Biomolecular and polymer features can be detected with high sensitivity, and application areas include biosensing and environmental monitoring.

Our design leverages two subgroups of gold bar antenna arrays, each of which consists of four microantennas with the same dimensions, as shown in the left panel of **Figure** 2a. Each microantenna can be viewed as a bright dipole resonator, and the neighbor pair of antennas gives rise to a dark quadrupole resonance, which is also called a symmetry-protected BIC.[45,46] Thus, it is not surprising that such a metasurface will support three degenerate symmetries-protected BICs with the same resonant frequency. If the lengths of the upper-left and bottom-right antennas are reduced from L to L_1 with a perturbation of $\Delta L_1 = (L - L_1)/2$ and the other antennas are fixed (see Figure 2a), one of the BICs is transformed into a QBIC with a finite and high Q-factor due to the broken symmetry, as demonstrated in Figure 2b. Following the same strategy, two QBICs can be excited by perturbing the lengths of two antennas in each subgroup. All three QBICs are triggered when four micro-antennas have different lengths. Multipole decomposition analysis shows that these QBICs are dominated by the electric dipole and magnetic quadrupole (Figure S4, Supporting Information). Here, we would like to point out that such a design has three advantages compared to other metasurfaces supporting BICs. First, multiple degenerate BICs can be supported with the same structure depending on the number of gold antennas. Therefore, one can excite multi-QBICs with different resonant frequencies by perturbing the length of the antenna in different degrees, which is beneficial to detecting various molecules with distinct responses in the THz range. Both the Q-factors and resonance frequencies can be tailored precisely by engineering the length of gold bars. Second, unlike most silicon metasurfaces operating in the THz range, the electric fields of QBICs are strongly localized near the structure instead of being confined within the structure, which is favorable for biosensing. Third, such compact metasurface-based devices have substantially reduced footprints compared to conventional dielectric-based integrated devices. The spatial advantage facilitates the seamless expansion toward multi-resonant metasurface photonic antennas, offering a convenient scalability option by integrating novel

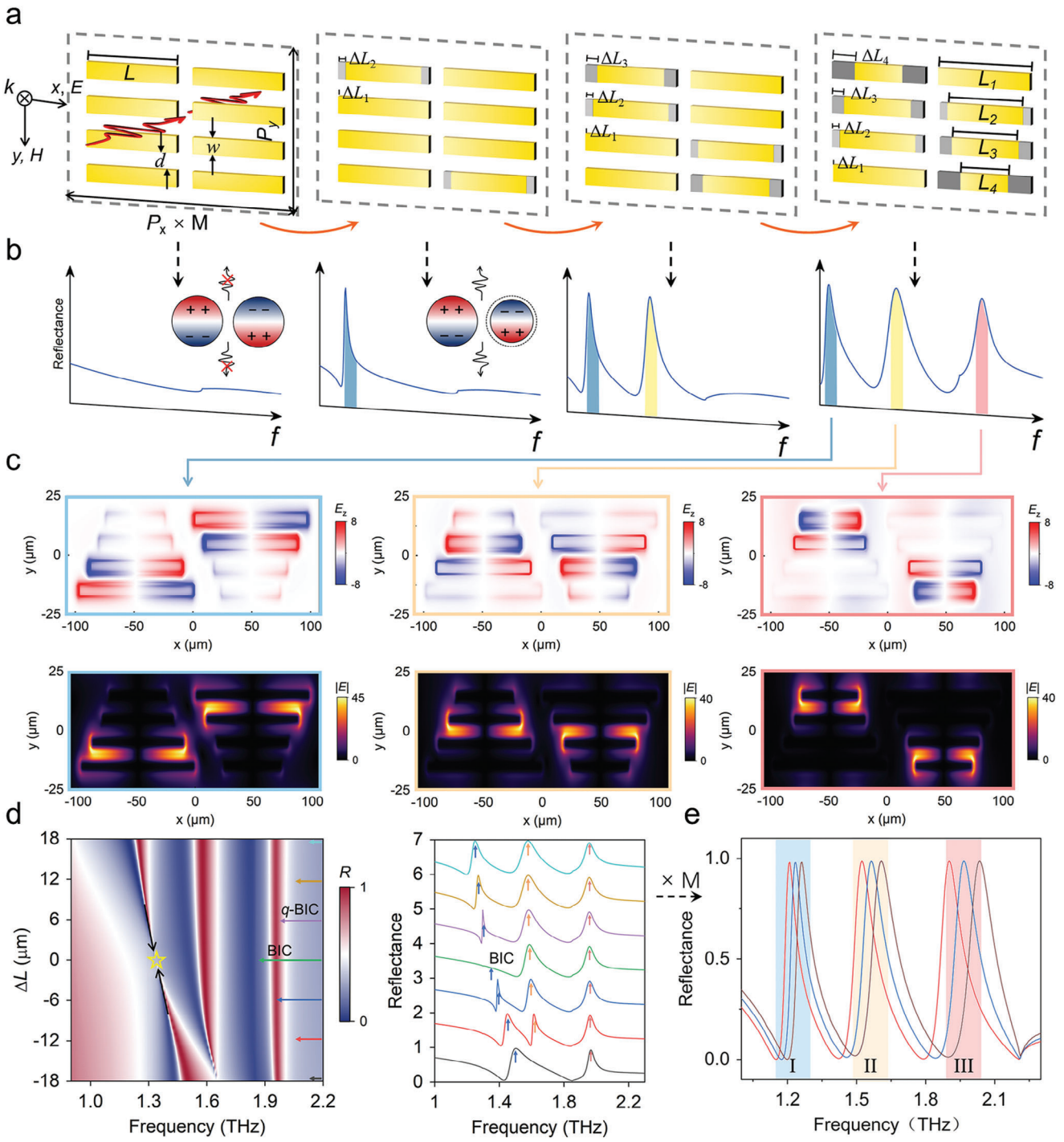

Figure 2. Design of multi-QBICs-based metal metasurfaces. a) Schematic illustration of multi-resonant metasurfaces whose unit cell is made of two subgroups of gold microantennas. The lengths of four bars are intentionally perturbed to create multi-QBICs. b) The corresponding reflection spectrum of the metasurfaces in (a). The insets are the mechanism of the interfering resonances for a resonating system. c) Structural response and electric field distributions of the three QBICs metasurface parallel to the substrate plane, corresponding to different resonance frequencies. d) Typical reflectance spectra mapping of the multi-resonant metasurface, with the geometrical parameters of the unit cell as follows: width w = 5 μm, gap d = 5 μm, and periodicity P_x = 220 μm, P_y = 50 μm, respectively. Maintaining the lengths of antennas L_2 = 82 μm, L_3 = 64 μm, and L_4 = 51 μm, while varying the length of L_1 from 64 μm to 100 μm. BIC point is labeled by yellow stares. e) Reflectance spectra of the multi-resonant (typical I, II, III, shaded areas) metasurface with scaled lateral (×M) dimensions. Detailed parameters of varying antennas in different pixelated areas are provided in Table S1 (Supporting Information).

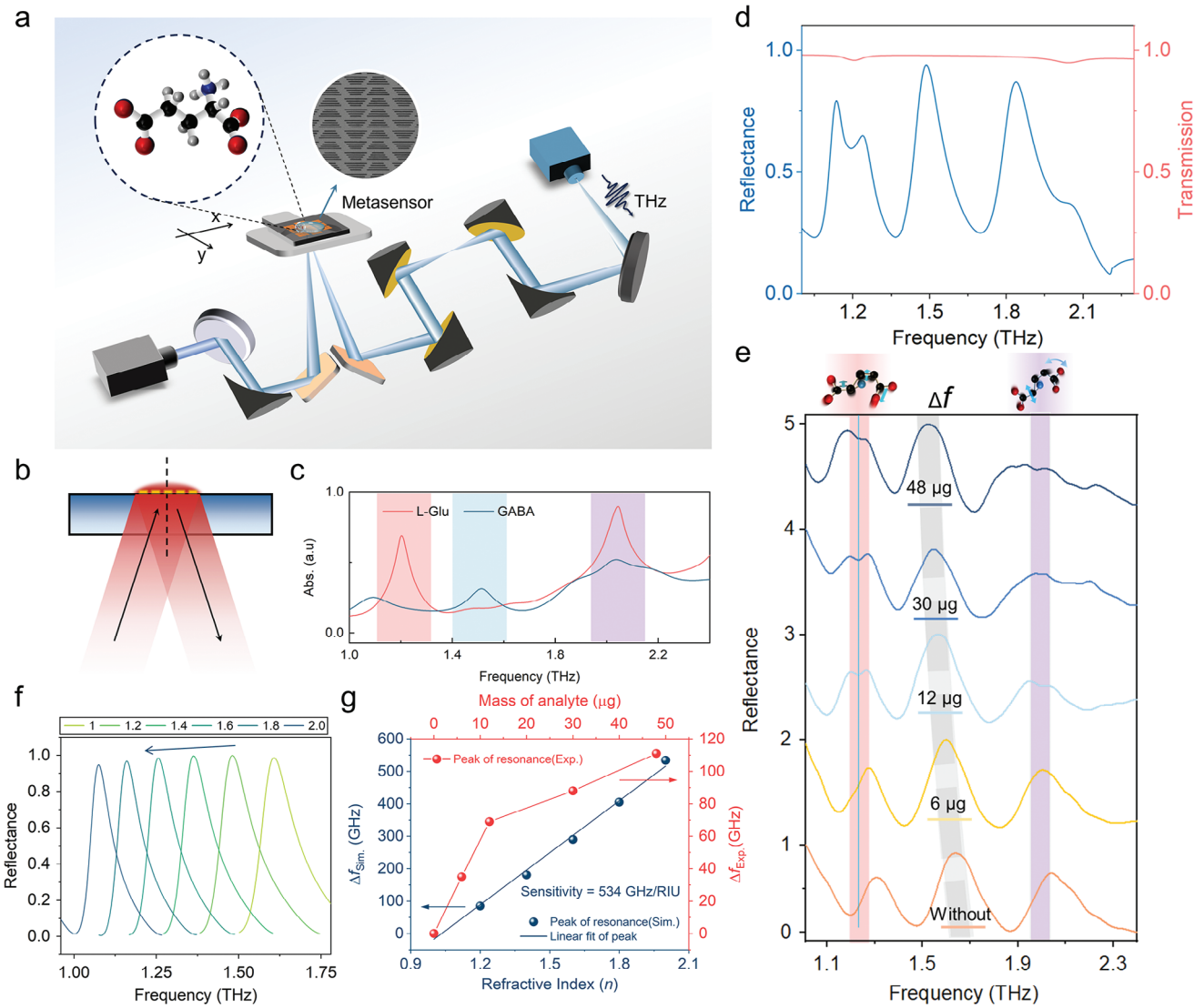

Figure 3. Simultaneous molecular fingerprint identification and quantitative analysis with multi-band plasmonic metasurfaces. a) Schematic diagram depicting the intricate configuration of the experimental setup. b) Basic geometry of a typical reflectance sampling technique. c) Graph showing the experimentally measured absorption spectra of two species from different classes of neurotransmitter-related biomolecules, highlighted with colored areas. d) Simulated reflectance spectrum of the multi-resonant metasurface for the nominal design with L-Glu. The additional dips in the peak lineshapes result from transmission under the same conditions. e) Measured reflectance spectra of the metasensor with varying trace amounts of L-Glu. The shaded area (red and purple) indicates the positions of absorption valleys, which agree with the simulation from d. The typical II resonance peak (gray stripe) exhibits a red shift with the increase of analytes. f) Simulated reflectance spectra with an analyte of semi-infinite thickness (Figure S7, Supporting Information) and refractive index n varied from 1 to 2 on the metasurface. g) Tip-to-tip resonance frequency shift versus the change in the refractive indices of the analyte (blue line). The metasensor sensitivity can reach 534 GHz/RIU. The frequency shift of the II is caused by a change in the amount of L-Glu (red line).

components into the available space whenever application demands arise.

As a concrete example, we design a THz metasurface that supports three QBICs with resonance frequencies ranging between 1.1 and 2.1 THz, which overlap with the optical responses of multiple absorption spectra of the analyte (L-Glu and GABA), as shown in Figure 3c. The other parameters of the unit cell are w = 5 μm, d = 5 μm, L_2 = 82 μm, L_3 = 64 μm, and L_4 = 51 μm. What makes this metasurface approach truly remarkable is its inherent flexibility to incorporate additional resonance bands, each meticulously tailored to align with specific spectral regions of interest. L_1 is continuously changed to observe the evolution from QBICs to BICs. Figure 2d (left panel) shows the reflection spectrum mapping as a function of L_1 and the frequency of incident waves. It is clearly seen that there are three QBICs (denoted as QBIC-I, QBIC-II, QBIC-III) featured by three high-Q Fano resonances across the spectrum range (Figure S5 and Table S2, Supporting Information). Figure 2c shows the eigenfield distributions of three QBICs. Furthermore, the electric fields of QBIC-I are mainly distributed around bottom-left and top-right bar pairs.

On the contrary, the electric field of QBIC-III is located near the top-left and bottom-right bar pairs. For QBIC-II, the electric fields are confined around the middle two bars for both left and right subgroups. We observe a significant ≈40-fold enhancement of the electric field in the near field. Note that the right two resonances behave as QBICs with finite Q-factors because the top three microantennas have different lengths. However, the left resonance evolved from QBICs to BIC as ΔL decreases from 18 to 0 μm. Further decreasing ΔL renders BICs become QBICs. The BIC is manifested by a Fano resonance with a vanished line width. The distinct feature of the narrowing of the leaky resonance is accompanied by abrupt π-phase changes of the electric field of the resonant metaatom lattice in the contour map (Figure S6, Supporting Information), which manifests itself as a narrow Fano resonance.[47] To better visualize the evolution process, seven typical reflectance spectra are selected and shown in the right panel of Figure 2d. The QBIC-III mode is generated by the coupling of adjacent microantennas L_3 and L_4, well isolated from another QBIC-I mode generated by the coupling of L_1 and L_2 (not directly coupled to either L_3 and L_4). Remarkably, the resonance line width gradually reduces to zero and then becomes broader as the asymmetry parameters vary from 18 to −18 μm. Another salient property of such a design is the resonance frequencies of three QBICs can be tuned linearly by scaling the dimensions along the *x*-axis, as demonstrated in Figure 2e. In the following section, we demonstrate that such metasurfaces can be used for detecting biomolecules in the THz range.

To corroborate our theoretical prediction, we fabricated a series of metasurfaces on the TPX substrate with conventional photolithography techniques. Specifically, 10 nm titanium as an adhesion layer and 100 nm gold are deposited in succession onto the TPX substrate by magnetron sputtering (see Experimental Section). The final pattern of metasurfaces is defined based on the standard photolithography process. The inset of **Figure 3a** shows the scanning electron microscopy (SEM) image of a typical fabricated metasurface. An overview of the experimental setup for measuring the reflectance spectrum is visually presented in Figure 3a,b. The sample stage, adopting a horizontally open configuration, is strategically positioned within the focal plane. This optimal placement ensures precise measurements and captures the essence of the THz reflectance spectrum from the array. To capture this spectrum, we employ a THz time-domain spectrometer, directing irradiation onto the chip from the back of the substrate, as diagrammed in Figure 3b. It is akin to revealing the hidden secrets of light and molecules, uncovering their dance on the stage of scientific inquiry. This provides the opportunity to inquire about the samples on the microantenna surface via surface-enhanced THz spectroscopy. Here, we select the L-Glu and GABA as the target analytes because they are involved in excitatory transmission and inhibitory regulation between neurons, respectively, and play an important role in the normal functioning of the central nervous system. We first use the transmission pressurized tablets technique to measure the absorption fingerprint spectra of our chosen analytes: L-Glu and GABA, as shown in Figure 3c. It can be observed that these two analytes have unique optical responses between 1.0 and 2.4 THz. More specifically, L-Glu I and II exhibit strong absorption ≈1.22 and 2.02 THz, respectively. For GABA I and II, absorption peaks occur at 1.53 and 2.02 THz. Thus, to effectively detect L-Glu and GABA, we intentionally design our metasurfaces to support multiple resonances at these target frequencies.

A typical calculated reflectance spectrum of the intentionally designed metasurface chip accompanied by the deposition of L-Glu (Figure S8, Supporting Information) is shown in Figure 3d. Since the resonance frequencies of QBIC-I and QBIC-III supported by the metasurfaces are perfectly overlapped with the absorption peaks of L-Glu, significant changes occur in the reflectance spectrum after coating L-Glu. Thanks to the high-Q nature of QBICs and their excellent field localization around the antenna, the absorption intensity obtained from our metasurface is almost one order higher than that directly measured using traditional transmission methods. Note that the full-frequency dispersive complex refractive index of the analyte has been taken into account during the simulation process. Besides, other analytes like GABA can be easily detected in a similar way as long as we align the resonance frequencies of multi-QBICs with the intrinsic absorption peaks of analytes. Figure 3e presents the reflectance spectra of our resonant metasurface after coating L-Glu with different concentrations. It can be found that the left resonance peak exhibits redshifts and splits into two peaks as the analytes increase. Therefore, both QBIC-I and QBIC-III can be used for recognizing characteristic absorption of molecules. In addition, the experimental results of multi-pixel metasurfaces decorated with analyte are shown in Figure S9 (Supporting Information).

For QBIC-III, it also shows a slight red shift and becomes more and more broadened. Additionally, although QBIC-II does not overlap with the characteristic absorption peaks of analytes, it still shows redshifts and can thus be used for refractive index sensing. As shown in Figure 3f,g, we simulated the reflectance spectrum that covers the second resonance when the metasurface is embedded into the background medium with a tunable refractive index. The resonance peak shows an obvious red shift with the increasing refractive index. To quantitatively characterize the performance of such a biosensor, we retrieve the resonance peaks at different *n* and plot them in Figure 3g. Applying linear fitting gives us a sensitivity of 534 GHz/RIU. Also, we plot the measured resonance peaks as a function of analyte mass. Reasonably good agreement can be found between experiments and simulations. However, it is not easy to compare the experimental measurements and simulation results because it might be challenging to establish the correspondence between the mass of the analyte and the refractive index of the background medium. In a word, such multi-resonant metasurfaces allow for simultaneously detecting absorption peaks of analytes and refractive index changes of the background medium.

Next, we experimentally validated the applicability of the THz PIR platform in monitoring molecular fingerprints affected by dynamic interactions that involve both polar and nonpolar molecules in the environment. The successful detection of characteristic alterations in affected analytes in aqueous media will facilitate efficient research on in situ light interactions with biomarkers, amino acids, proteins, and other substances. To conduct real-time in situ measurements, we continuously monitor the reflectance spectrum. In numerous previous studies focusing on trace sensing, it has been customary to analyze analytes in a desiccated state.[48,18] Nevertheless, in practical detection scenarios, the chemical environment exerts a substantial influence

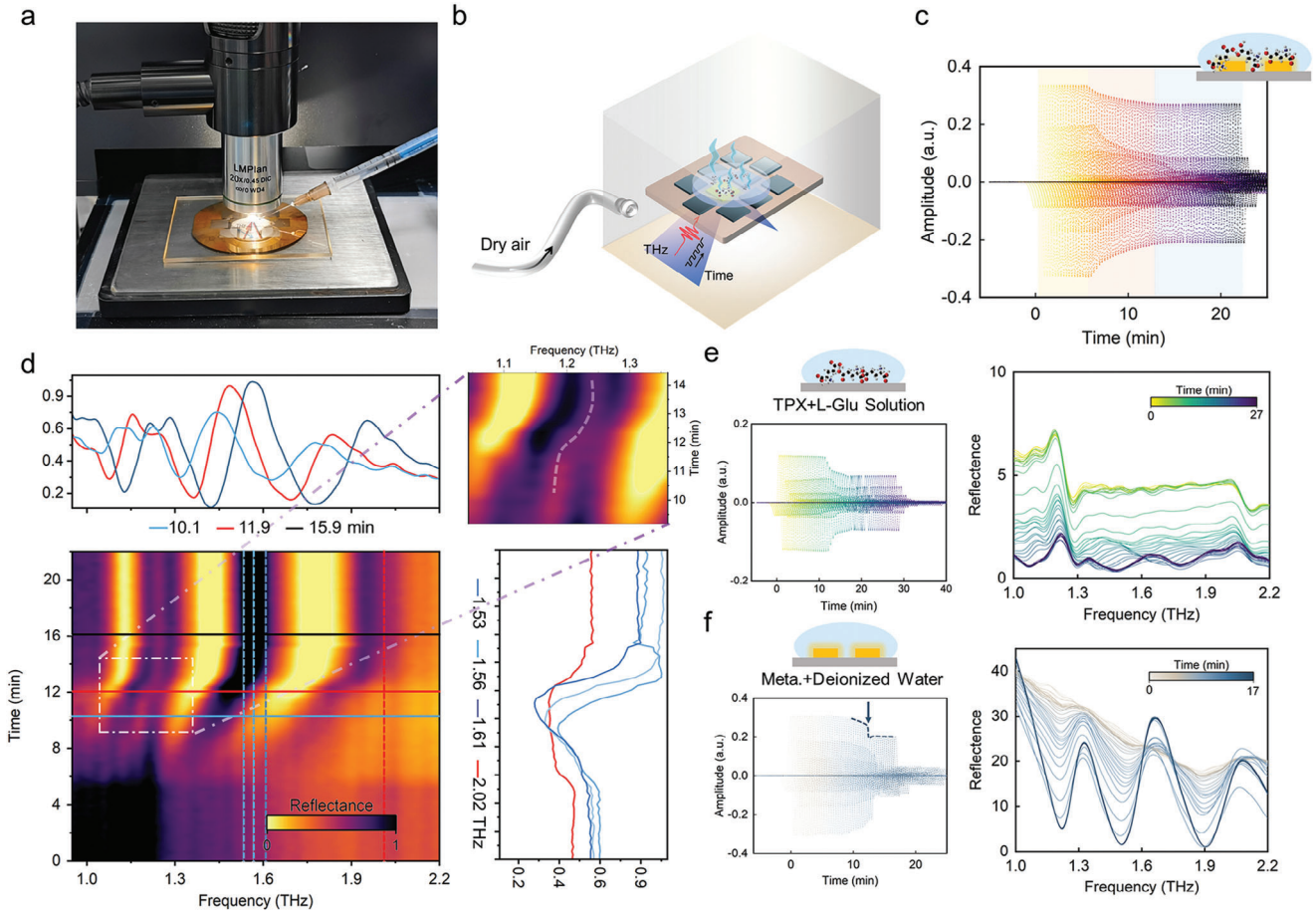

Figure 4. Molecular absorption fingerprinting was monitored in real-time and in situ with the THz plasmonic internal reflection (PIR) platform. a) The setup utilized for in situ micro-THz PIR bioexperiments in water. A plasmonic chip is integrated into a TPX device clamped below the objective. The optical path is on the lower side under the TPX platform and is shown in Figure 3a. The microscope on the upper side is used to observe the metasurface and loaded biological sample conditions. b) Schematic of the experimental configuration. A diagram illustrates the dynamic monitoring of analyte variations on the metasurface, providing real-time data. c) The stable reflectance real-time signal of the metasurface is continuously collected as the L-Glu-containing solution evaporates. The process includes three main stages (yellow, red, and blue ribbons). d) The normalized reflectance spectra are obtained through the Fourier transform of the time-domain signal of different stages in c. The inset graph magnifies a specific area marked by a white dashed box. The white dashed line shows the trajectory of absorption frequency variation. On the top, experimental slices at three representative moments demonstrate the evolution of the spectrum. On the left, the intensity evolution at four representative frequencies is displayed. e,f) The reflectance spectra of different scenarios, without metasurface, or the absence of the analyte, were as controlled experiments. The blue arrow in the left panel of (f) indicates the moment of rupture of the water film on the metasurface.

on the structure, function, and interactions of analyte molecules. Hence, to address this practical issue, we embarked on a further exploration into the influence of solvent evaporation on the characteristics of analytes, particularly their absorption fingerprints. **Figure** 4a,b elucidates the experimental setup employed in our investigation. By continuously injecting dry air, the environmental conditions surrounding the chip can be consistently maintained at a humidity level below 3%. Leveraging the real-time capabilities of our reflectance method, an extensive collection of spectro-temporal data is amassed.

The real-time measurement of THz reflectance time spectra is depicted in Figure 4c. As the water gradually evaporates, the effective refractive index of the sample coating the sensor's surface steadily increases, leading to a progressive attenuation of the reflected signal's amplitude at the interface in accordance with Snell's law. Eventually, as the water in the L-Glu solution is entirely depleted, a reflection signal of unwavering intensity becomes evident.

Subsequently, we further analyze the changes in molecular oscillation modes during this process. The dynamic behavior is reflected in characteristic absorption spectra. Therefore, we perform the Fourier transform on a vast amount of spectro-temporal data collected in real-time format of reflectance-based methods to obtain reflectance spectra with absorption features in Figure 4d. The results clearly depict the change process of the L-Glu I absorption fingerprint during solvent evaporation. The process mainly includes three stages: With sufficient solvent, solvent molecules can surround and interact with solute molecules to form a solvated layer. The solvation layer stabilizes the structure and vibration of the solute molecules, reducing their exposure to the external environment. However, the inclusion of solvent molecules leads to a redshift in the resonance frequency of solute

molecules. This redshift occurs because the presence of solvent molecules alters the electron distribution of solute molecules, weakening the resonance phenomenon and thus reducing the resonance frequency.

In solution, the effect of the water evaporation process on the molecular resonance frequency can be elucidated by the solvent effect.[49,50] The solvent effect is the environmental impact of solvent molecules on solute molecules, including the interaction between solvent molecules and solute molecules. The solvent effect is described by the Kirkwood–Buff theory, according to which the effect of solvent molecules on solute molecules can be qualitatively expressed by the polarization energy of solvent molecules.[51]

$$\Delta\nu \sim -\kappa\Delta\varepsilon \tag{1}$$

where $\Delta\nu$ represents the change in the resonant frequency of the molecule, κ denotes an experimental parameter characterizing the extent of the solvent effect on the resonance frequency of the molecule, and $\Delta\epsilon$ indicates the alteration in the polarization energy of the solvent.[52] This equation expression effectively describes the overall impact of solvent effects on the molecular resonance frequency.

There is a relationship between the amount of polarization energy change of the solvent and the solvent amount. In general, as the solvent amount increases, the amount of polarization energy change of the solvent also increases. This is due to the increased interaction between the solvent molecules and the solute molecules, resulting in an increase in the polarization energy of the solvent molecules. From Figure 4d, putting L-Glu into water redshifted the resonance frequency from 2.02 THz in the solid powder state to 1.17 THz in the solution state. As can be seen in Figure S10 (Supporting Information), the molecular (L-Glu) absorption fingerprints in a sufficient amount of nonpolar fluorine oil also can be clearly tested that a redshift has occurred.

It should be noted that the amount of change in the polarization energy of a solvent is also affected by other factors, such as the polarity of solute and solvent molecules, as well as the interaction between solvent molecules. Therefore, the relationship between the amount of change in the polarization energy of a solvent and the amount of solvent is not a simple linear relationship but requires a combination of several factors. Further, we executed control experiments as detailed in Figure 4e. It is perceptible that the characteristic absorption fingerprints of the molecules change in the absence of the metasurface, albeit to a minor extent. The directional shift in change remains highly consistent with the case involving the metasurface. Upon complete evaporation of the solvent, the molecular vibration frequencies may undergo significant variations due to structural modifications and energy redistribution within the molecules.

The outcomes of this study will enrich our comprehension of the dynamics of analyzing characteristic fingerprints in the THz band within a solution, as well as the selection and optimization of solvents. Furthermore, the solvent content can be predicted by pinpointing the specific position of the fingerprint. This experimental setup paves the way for novel territories in in situ real-time dynamic detection in biochemistry in the THz band. By eliminating the traditional time-consuming drying procedures, this approach streamlines biosensing and enhances its versatility in diverse scenarios.

We further demonstrate the capability of monitoring and distinguishing multiple biological analytes simultaneously at a steady state for a THz plasmonic biosensor. In addition to L-Glu, we chose to study another biomolecular GABA, which plays an important role in the treatment and prediction of a wide range of complex neurological diseases and psychiatric disorders.[53,54] Specifically, we target the L-Glu I and II bands located at ≈1.22 and 2.02 THz as well as GABA I and II located at ≈1.53 and 2.02 THz (Figure S11, Supporting Information). The schematic diagram of mixing L-Glu and GABA is shown in **Figure 5a**. L-Glu/GABA mixtures with several mixing ratios are executed in Figure 5b. Figure 5c,d shows the reflectance spectra with several mixing ratios, from which we can accurately identify the components in a mixture even if they have almost the same absorption fingerprint (GABA II and L-Glu II). In addition, the proportions of the mixtures can be judged by the absorption strength. To confirm that the two reference spectra used are sufficient to capture the full biological information in our weight measurement, we performed principal component analysis (PCA, Figure 5e) over the spectral data corresponding to all the ratio data (see Experimental Section).[55–57] The principal component loadings and explained variance are shown in Figure S12 (Supporting Information). In Figure 5e, each cluster represents a mixing ratio. Since there is no overlap between each cluster, we can achieve the classification of different mixture ratios. Next, molecular identification is performed using support vector machines (SVM). The dataset imported into SVM is 50 spectra of each mixing ratio, randomly divided into 40 training datasets and 10 testing datasets. The linear kernel function is used as the kernel of SVM. Finally, we obtained 100% recognition accuracy for each set of mixing ratios (Figure 5f).

To capture the changes in analyte concentration more comprehensively and improve the accuracy of prediction, we established a mixed analyte proportion prediction regression model using a multimodal deep neural network (MM-DNN).[58] MM-DNN contains three layers, which are the input layer, hidden layer, and output layer (Figure 5h). The MM-DNN model contains 2 hidden layers, each hidden layer has 64 nodes. The output layer consists of 2 nodes, corresponding to the number of species in the sample. Next, the reflectance spectra in Figure 5d are imported into the MM-DNN model as a training set. The loss after training is 1.36 and the accuracy is 91.11% (Figure S13, Supporting Information). In addition, we calculated the precision and recall to evaluate the performance of the model. Through calculation, the precision of the deep learning model is 92.56% and the recall is 91.11%. This result shows that the model has good classification ability and recognition ability for target samples. Then, the newly obtained measured spectral data (Figure 5g) is input into the trained MM-DNN model as a test set. Figure 5i shows the concentration predictions of all components in the output mixture. The predicted results are very close to the actual results. It should be emphasized that our platform is not limited to two biochemical species and can be extended to bioassays with a higher number of biological components, as well as to explore unknown samples or analytes with unknown absorption spectra, through the inclusion of the corresponding reference spectra in the analysis of the PCA method with universal applicability. This

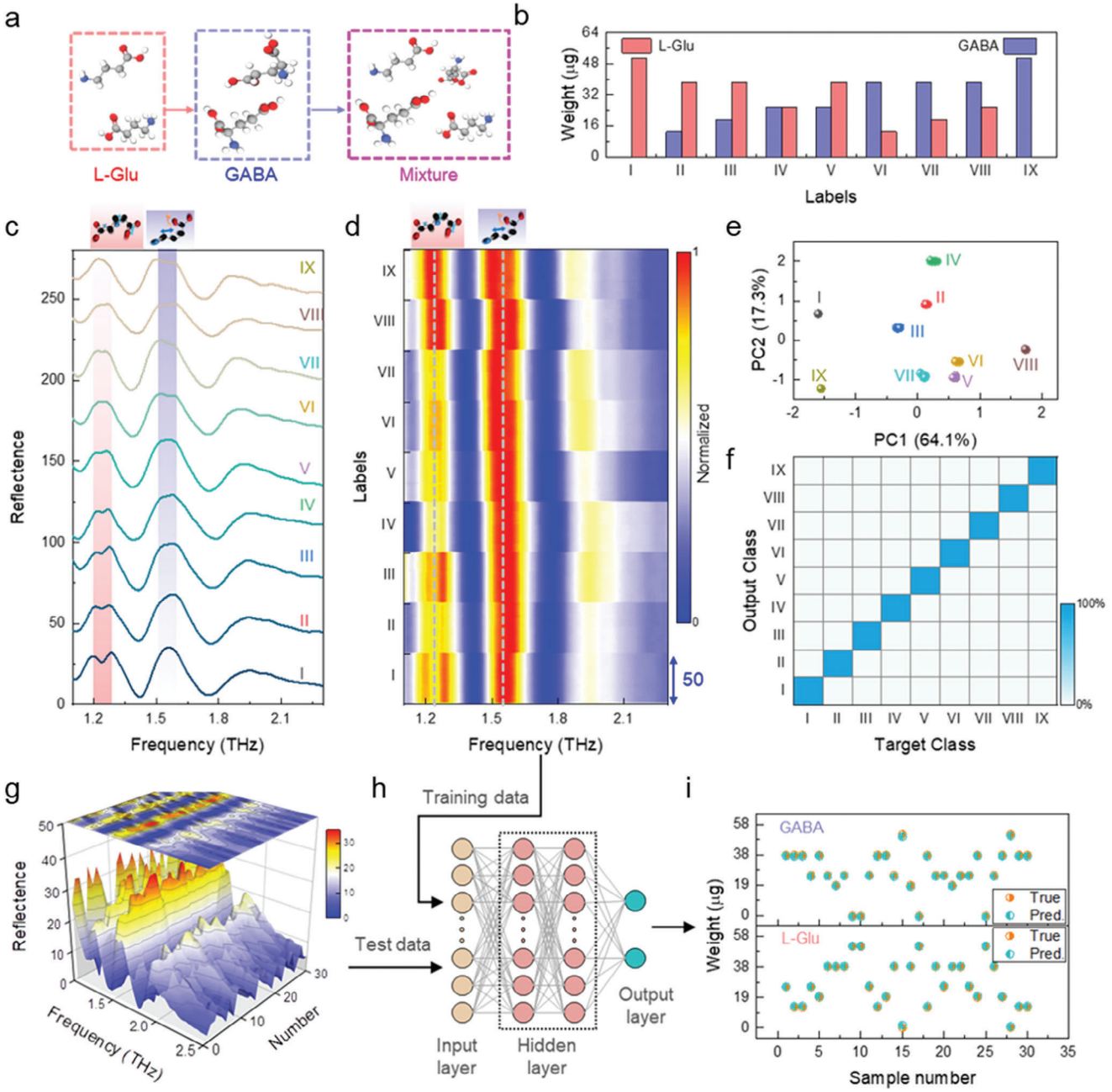

Figure 5. Classifying mixed samples and predicting concentrations. Machine learning assisted multi-resonant THz platform for classification and accurate prediction from mixed samples. a) Schematic diagram of mixing L-Glu, and GABA. b) The bar plot of the titrated concentration mixes of L-Glu and GABA. c) The reflectance spectra of the multi-resonant THz platform under different analyte mixing conditions. d) The reflectance spectra of sensing data with different analyte states. Each mixing state contains 50 sets of reflectance spectra. e) The weight of scores of each spectrum in a 2D space after PCA. f) The confusion map of machine learning results indicates 100% accuracy in mixed analyte identification. g) Reflectance spectra under different analyte mixing conditions as a test set. h) The multimodal deep neural network (MM-DNN)-based regression model for mixed analyte concentration prediction. i) Concentration prediction results corresponding to the data in (g).

molecular-specific and label-free detection method enables precise analysis of absorption fingerprints, thereby opening up exciting avenues for the study of biological effects within the THz band. Our findings contribute to the advancement of THz absorption spectroscopy as a transformative tool for understanding and investigating complex biological phenomena.

3. Conclusion

THz absorption spectroscopy emerges as a formidable technique for elucidating the intricate details of molecular vibration information in a label-free manner. This technique is crucial for unraveling the complexity inherent in biological processes,

allowing for the differentiation of various fundamental biomolecules and their interactions. We have developed a novel multi-band THz plasmonic biosensing platform capable of providing label-free resolution of molecular specificity fingerprint information. The structural design incorporates self-similar multi-QBICs to achieve independently regulated simultaneous enhancement of multiple spectral points, which can effectively improve the accuracy and precision of analyte identification. Moreover, the sensor allows in situ and real-time monitoring of the dynamic changes in the vibrational modes of solute molecules in solution as the solvent evaporates. These findings demonstrate that our developed technology provides an advanced experimental solution for studying the dynamic biological effects associated with neurotransmitter molecules in the THz range. It is also important to note that the reflective, real-time approach enables the stable collection of a large amount of spectral time-domain datasets, which makes it possible to construct deep neural networks to accurately discriminate and predict the composition and proportions of various mixtures. Extending this configuration to more complex fingerprint dynamics detection and mixture substance identification, we then leverage our method to monitor neurotransmitter cargo release from synaptic vesicles in response to specific drug-induced releases, providing a new approach to drug development for brain-related disorders as well as exciting applications of THz in neural signaling modulation.

The proposed approach makes a significant contribution to the field of broadband-enhanced absorption spectroscopy research (Table S3, Supporting Information), especially in analyzing specific molecules in heterogeneous systems as well as in dynamic real-time tracking, showing great potential for applications. In addition, we anticipate that multi-band pixelated metasurfaces will be widely used in the design of various 2D-functionalized material platforms, and their ubiquity lays the foundation for realizing a wider range of applications.

Improving the detection range is crucial to further advance the technology. Different molecules and biological systems may have characteristic absorption bands in multiple spectral ranges, so attempts can be made to combine other bands (e.g., mid-infrared) to design multimodal sensing platforms for comprehensive monitoring of complex biological processes. In addition, in order to meet the demand for detecting more trace target substances, further breakthroughs in the lower detection limit of the platform are needed to improve the highly sensitive detection of trace analytes. Although the designed metasensors have demonstrated the advantages of miniaturization, achieving large-scale production and standardized use imposes higher demands on the miniaturization of the devices. In this regard, plasmonic microantenna structures offer unique advantages in terms of scalability and miniaturization and can provide new avenues for the development of miniaturized micro- and nanophotonic biosensors.

4. Experimental Section

Numerical Simulations: The reflectance spectra and near-field electric distributions of the microantenna arrays were computed using the Finite-Difference Time-Domain (FDTD) method implemented in the Lumerical FDTD software. The periodicity of the arrays was accounted for through the utilization of periodic boundary conditions defining the unit cell of the array. The structure was excited by illuminating it with a plane wave aligned with the dipole microantennas and incorporating all propagating Floquet modes. Additionally, the platform accommodated normal incidence of light on its backside. The scattering characteristics were computed on a refined mesh iteratively until convergence was achieved. The default simulation environment was usually ideal dry air (no water, background refractive index of 1, simulated temperature of 300 K).

Metasensor Microfabrication—Substrate Preparation: The platform substrate underwent a combination of injection molding and precise engraving to achieve the desired dimensions. This was done using a polymer material with a refractive index of ≈1.46. Subsequently, the substrate was cleansed with deionized water and ethanol. To ensure a pristine surface and enhance adhesion during metal deposition, the substrate was then dried using a gentle stream of nitrogen gas.

Metasensor Microfabrication—Photolithography: The photoresist was spin-coated onto the substrate and gently baked. The pattern of the mask plate was then transferred to the photoresist coating by UV irradiation. The exposed substrate was reacted in a specific developer, taking care to control the important parameter of development time. Specific wavelengths of light were used in conjunction with the corresponding developer to ensure effective exposure and development.

Metasensor Microfabrication—Metal Deposition: Sequentially, a 10 nm chromium layer followed by a 100 nm gold layer was deposited onto the cleaned silicon substrate. These layers were deposited using a magnetron sputtering system.

Metasensor Microfabrication—Lift-off Process: To delicately remove the photoresist layer and the gold film adhered to the upper rim, the coated samples were submerged in acetone. Ultrasonic debonding was employed with greater efficacy to maintain the integrity of the metal microstructure, aiming to prevent any undesired impairment.

THz Spectroscopy System Measurements: To acquire spectroscopic data, the advanced TAS7500TS THz ultra-broadband spectroscopy system, crafted by Advantest Co., Ltd in Tokyo, Japan, was utilized. This exceptional apparatus featured a frequency range spanning from 0.5 to 7.0 THz, showcasing a remarkable frequency precision of 3.8 GHz. It comprised crucial components such as a femtosecond laser, two photoconductive antennas serving as both THz emitters and detectors, a precision time delay device, and data collection software. This setup enabled precise measurements, yielding detailed and accurate results. The method entailed the strategic utilization of a pair of optical fiber lasers operating at a wavelength of 1550 nm, each with pulse durations beneath 50 *f*s. Operating at a repetition rate of 50 MHz, one laser transmitted the sample while the other detected the THz signals. With a system noise level below 60 dB, the system enabled measurements in both normal reflectance and transmission modes in the time domain. In this work, in order to facilitate experimental operations and dynamic monitoring, reflective modules were used for data collection.

Data Collection and Analysis Process: The photoconductive antenna method was utilized to generate and detect THz signals operating in reflection mode. By using an advanced phase-modulated dual-laser synchronization control method, time-domain signals that contain analytical details were collected. The emitted THz signals were polarized in a transverse magnetic (TM) mode and focused onto the plane of the sample stage where the metasensor was placed. During the experiment, the THz signal was incident from the backside at a low fixed angle of 5° onto the test platform. The electric field of the THz signal was consistently parallel to the long axis of the miniature antenna. To ensure accurate sensing results and to minimize the effect of water in the environment, an air dryer was used to dry the experimental environment, keeping the relative humidity below 3%. The environment was dried for 30 min before starting data measurements. The signal of the THz pulse through the bare TPX substrate was used as the reference signal. In the post-processing step, the time-domain signals of the THz pulses measured through the metasurface adorned with the analyte (Figure 4c) were subjected to a fast Fourier transform (FFT) to obtain the corresponding THz spectrum. Then, the THz spectrum reflected through the analyte ($R_{S(\omega)}$) is normalized with the spectrum

reflected only from the substrate ($R_{R(\omega)}$), i.e., $R_{(\omega)} = |R_{S(\omega)}/R_{R(\omega)}|$, and the normalized spectrum is shown in Figure. 3e.

Machine Learning: In mixed sample classification, PCA was employed for dimensionality reduction of measured spectral data. To facilitate the visualization of the feature space, PCA was performed in OriginPro 2018. A correlation matrix was calculated for the normalized set of features, from which eigenvectors and eigenvalues were extracted to construct principal components as linear combinations of the initial features. The first two principal components were used to display a 2D scatterplot of the features. The proposed SVM classifiers were developed on Python 3.6 using the scikit-learn package. The entire dataset comprised 450 spectra, and the dataset was split into training data (80%) and testing data (20%). The linear kernel function was used as the kernel of the SVM with a C set to 1. For concentration prediction, an MM-DNN model was developed using the scikit-learn package based on Python 3.6. The MM-DNN model consisted of feature concatenation and a Deep Neural Network (DNN) architecture. Early fusion was employed to combine features from metasurface and molecular data into a unified representation. Subsequently, feature extraction and dimensionality reduction were applied to the fused dataset. The architecture of the DNN model was composed of fully connected layers that utilize Rectified Linear Unit (ReLU) activation functions. MM-DNN leveraged Keras to define a sequential model for regression tasks with two output nodes. The model architecture included an input layer, hidden layers, and an output layer. The input layer consisted of 315 nodes, corresponding to the frequency points within the spectral range. The model contained two hidden layers, each comprising 64 neurons. These hidden layers enabled the model to discern complex relationships and facilitate precise predictions. The output layer consisted of two neurons with a linear activation function, providing regression outputs for two target variables. The model was compiled using the Adam optimizer with a Mean Squared Error (MSE) loss function. Additionally, metrics such as mean absolute error (MAE) and accuracy were included to monitor performance. The Adam optimizer was a robust optimization algorithm that dynamically adjusted the learning rate based on the gradient of the loss function, enhancing training efficiency. During the entire training process, the model iteratively fine-tuned the weights and biases within the layers to minimize the loss function, ultimately improving prediction accuracy.

Supporting Information

Supporting Information is available from the Wiley Online Library or from the author.

Acknowledgements

R.W., R.H., D.L., and L.H. contributed equally to this work. This work was supported by the National Natural Science Foundation of China (Grant. 62305394); Distinguished Scholar of National Science Fund of China (No. 12225511) and Major Project (T2241002), Australian Research Council (Grant DP210101292) and the International Technology Center Indo-Pacific (ITC IPAC). [Correction added on March 10, 2025, after first online publication: Acknowledgement Section has been updated.]

Conflict of Interest

The authors declare no conflict of interest.

Data Availability Statement

The data that support the findings of this study are available in the supplementary material of this article.

Keywords

biosensors, deep learning, microplasmonics, resonances metasurfaces, terahertz spectroscopy

Received: November 21, 2024
Revised: February 4, 2025
Published online:

[1] H. Altug, S.-H. Oh, S. A. Maier, J. Homola, *Nat. Nanotechnol.* **2022**, *17*, 5.
[2] D. Rodrigo, A. Tittl, N. Ait-Bouziad, A. John-Herpin, O. Limaj, C. Kelly, D. Yoo, N. J. Wittenberg, S.-H. Oh, H. A. Lashuel, H. Altug, *Nat. Commun.* **2018**, *9*, 2160.
[3] H. Zhou, X. Hui, D. Li, D. Hu, X. Chen, X. He, L. Gao, H. Huang, C. Lee, X. Mu, *Adv. Sci. (Weinh)* **2020**, *7*, 2001173 .
[4] Y. Bi, C. Yang, Y. Chen, S. Yan, G. Yang, Y. Wu, G. Zhang, P. Wang, *Light: Sci. Appl.* **2018**, *7*, 81.
[5] S. Chen, Y. Zhang, T.-M. Shih, W. Yang, S. Hu, X. Hu, J. Li, B. Ren, B. Mao, Z. Yang, Z. Tian, *Nano Lett.* **2018**, *18*, 2209.
[6] M. Manoccio, M. Esposito, E. Primiceri, A. Leo, V. Tasco, M. Cuscuna, D. Zuev, Y. Sun, G. Maruccio, A. Romano, A. Quattrini, G. Gigli, A. Passaseo, *Nano Lett.* **2021**, *21*, 6179.
[7] Y. Chen, C. Zhao, Y. Zhang, C. W. Qiu, *Nano Lett.* **2020**, *20*, 8696.
[8] W. J. Choi, K. Yano, M. Cha, F. M. Colombari, J.-Y. Kim, Y. Wang, S. H. Lee, K. Sun, J. M. Kruger, A. F. Moura, N. A. Kotov, *Nat. Photonics* **2022**, *16*, 366.
[9] B. Ng, S. M. Hanham, J. Wu, A. I. Fernndez-Domnguez, N. Klein, Y. F. Liew, M. B. H. Breese, M. Hong, S. A. Maier, *ACS Photonics* **2014**, *1*, 1059.
[10] T. Ha, D. Yoo, C. Heo, F. Vidal-Codina, N.-C. Nguyen, K. I. Sim, S. H. Park, W. Cha, S. Park, J. Peraire, T.-T. Kim, Y. H. Lee, S.-H. Oh, *Nano Lett.* **2022**, *22*, 10200.
[11] S. Liu, S. Bai, Y. Wen, J. Lou, Y. Jiang, Y. Zhu, et al., *Science* **2025**, *387*, 202.
[12] X. Chen, S. Xin, Q. Liu, Y. Meng, D. Yu, M. L. Tseng, L Ye, *Nanophotonics* **2025**.
[13] Y. Meng, J. Feng, S. Han, Z. Xu, W. Mao, T. Zhang, J. S. Kim, I. Roh, Y. Zhao, D.-H. Kim, Y. Yang, J.-W. Lee, L. Yang, C.-W. Qiu, S.-H. Bae, *Nat. Rev. Mater.* **2023**, *8*, 498.
[14] S. Ye, K. Zhong, Y. Huang, G. Zhang, C. Sun, J. Jiang, *J. Am. Chem. Soc.* **2024**, *146*, 2663.
[15] Y. Huang, S. Zhong, Y.-C. Shen, Y. Yu, D. Cui, *Nanoscale* **2018**, *10*, 22466.
[16] Y. Huang, S. Zhong, T. Shi, Y.-C. Shen, D. Cui, *Opt. Express* **2019**, *27*, 34067.
[17] A. Ahmadivand, B. Gerislioglu, R. Ahuja, Y. Kumar Mishra, *Mater. Today* **2020**, *32*, 108.
[18] Y. Peng, C. Shi, Y. Zhu, M. Gu, S. Zhuang, *PhotoniX* **2020**, *1*, 12.
[19] R. Wang, Q. Wu, Y. Zhang, X. Xu, Q. Zhang, W. Zhao, B. Zhang, W. Cai, J. Yao, J. Xu, *Appl. Phys. Lett.* **2019**, *114*, 121102.
[20] L. Sun, L. Xu, J. Wang, Y. Jiao, Z. Ma, Z. Ma, C. Chang, X. Yang, R. Wang, *Nanoscale* **2022**, *14*, 9681.
[21] Y. Kivshar, *Nano Lett.* **2022**, *22*, 3513.
[22] N. Yu, F. Capasso, *Nat. Mater.* **2014**, *13*, 139.
[23] N. Yu, P. Genevet, M. A. Kats, F. Aieta, J. P. Tetienne, F. Capasso, Z. Gaburro, *Science* **2011**, *334*, 333.
[24] Y. Meng, Y. Chen, L. Lu, Y. Ding, A. Cusano, J. A. Fan, Q. Hu, K. Wang, Z. Xie, Z. Liu, Y. Yang, Q. Liu, M. Gong, Q. Xiao, S. Sun, M. Zhang, X. Yuan, X. Ni, *Light: Sci. Appl.* **2021**, *10*, 235.
[25] Y. Meng, Z. Liu, Z. Xie, R. Wang, T. Qi, F. Hu, H. Kim, Q. Xiao, X. Fu, Q. Wu, S.-H. Bae, M. Gong, X. Yuan, *Photonics Res.* **2020**, *8*, 564.
[26] A. Aigner, T. Weber, A. Wester, S. A. Maier, A. Tittl, *Nat. Nanotechnol.* **2024**, *19*, 1804.
[27] P. Jangid, F. U. Richter, M. L. Tseng, I. Sinev, S. Kruk, H. Altug, Y. Kivshar, *Adv. Mater.* **2024**, *36*, 2307494.

[28] N. Zhang, F. Gao, R. Wang, Z. Shen, D. Han, Y. Cui, L. Zhang, C. Chang, C.-W. Qiu, X. Chen, *Adv. Mater.* **2025**, *37*, 2411490.
[29] F. Neubrech, C. Huck, K. Weber, A. Pucci, H. Giessen, *Chem. Rev.* **2017**, *117*, 5110.
[30] Y. Chang, D. Hasan, B. Dong, J. Wei, Y. Ma, G. Zhou, K. W. Ang, C. Lee, *ACS Appl. Mater. Interfaces* **2018**, *10*, 38272.
[31] S. Ansaryan, Y.-C. Liu, X. Li, A. M. Economou, C. S. Eberhardt, C. Jandus, H. Altug, *Nat. Biomed. Eng.* **2023**, *7*, 943.
[32] C. W. Hsu, B. Zhen, A. D. Stone, J. D. Joannopoulos, M. Soljai, *Nat. Rev. Mater.* **2016**, *1*, 16048.
[33] J. Jin, X. Yin, L. Ni, M. Soljacic, B. Zhen, C. Peng, *Nature* **2019**, *574*, 501.
[34] L. Xu, M. Rahmani, Y. Ma, D. A. Smirnova, K. Z. Kamali, F. Deng, Y. K. Chiang, L. Huang, H. Zhang, S. Gould, D. N. Neshev, A. E. Miroshnichenko, *Adv. Photon.* **2020**, *2*, 11.
[35] L. Huang, L. Xu, D. A. Powell, W. J. Padilla, A. E. Miroshnichenko, *Phys. Rep.* **2023**, *1008*, 1.
[36] T. A. Andreas, Leitis, L. Mingkai, Y. Filiz, C. D. Duk-Yong, N. Neshev, S. K. Yuri, A. Hatice, *Science* **2018**, *360*, 1105.
[37] X. Zhao, C. Chen, K. Kaj, I. Hammock, Y. Huang, R. D. Averitt, X. Zhang, *Optica* **2020**, *7*, 1548.
[38] L. Cong, R. Singh, *Adv. Opt. Mater.* **2019**, *7*, 1900383.
[39] R. Wang, L. Xu, L. Huang, X. Zhang, H. Ruan, X. Yang, J. Lou, C. Chang, X. Du, *Small* **2023**, *19*, 2301165.
[40] R. Wang, L. Song, H. Ruan, Q. Yang, X. Yang, X. Zhang, R. Jiang, X. Shi, A. P. Shkurinov, *Research (Wash D C)* **2024**, *7*, 0483.
[41] R. Wang, L. Xu, J. Wang, L. Sun, Y. Jiao, Y. Meng, S. Chen, C. Chang, C. Fan, *Nanoscale* **2021**, *13*, 18467.
[42] J. Wei, Y. Li, Y. Chang, D. M. N. Hasan, B. Dong, Y. Ma, C. W. Qiu, C. Lee, *ACS Appl. Mater. Interfaces* **2019**, *11*, 47270.
[43] W. Xu, L. Xie, Y. Ying, *Nanoscale* **2017**, *9*, 13864.
[44] D. Rodrigo, A. Tittl, A. John-Herpin, O. Limaj, H. Altug, *ACS Photonics* **2018**, *5*, 4903.
[45] K. Koshelev, S. Lepeshov, M. Liu, A. Bogdanov, Y. Kivshar, *Phys. Rev. Lett.* **2018**, *121*, 193903.
[46] L. Khner, L. Sortino, R. Bert, J. Wang, H. Ren, S. A. Maier, Y. Kivshar, A. Tittl, *Nat. Commun.* **2022**, *13*, 4992.
[47] D. R. Abujetas, N. Hoof, S. Huurne, J. Gómez Rivas, J. Sánchez-Gil, *Optica* **2019**, *6*, 996.
[48] A. Ahmadivand, B. Gerislioglu, Z. Ramezani, A. Kaushik, P. Manickam, S. A. Ghoreishi, *Biosens. Bioelectron* **2021**, *177*, 112971.
[49] Cramer, J. Christopher, Truhlar, G. Donald, *Chem. Rev.* **1999**, *99*, 2161.
[50] S. T. Russell, A. Warshel, *Quart. Rev. Biophys.* **1984**, *17*, 283.
[51] V. Pierce, M. Kang, M. Aburi, S. Weerasinghe, P. E. Smith, *Cell Biochem. Biophys.* **2008**, *50*, 1.
[52] R. Giernoth, in *Solvents and Solvent Effects in Organic Chemistry*, 4th Ed (Eds.: C. Reichardt, T. Welton), Wiley, Verlag **2010**.
[53] Y.-F. Li, *Pharmacol. Ther.* **2020**, *208*, 107494.
[54] A. Reiner, J. Levitz, *Neuron* **2018**, *98*, 1080.
[55] D. Li, H. Zhou, Z. Chen, Z. Ren, C. Xu, X. He, T. Liu, X. Chen, H. Huang, C. Lee, X. Mu, *Adv. Mater.* **2023**, *35*, 2301787.
[56] Z. Ren, Z. Zhang, J. Wei, B. Dong, C. Lee, *Nat. Commun.* **2022**, *13*, 3859.
[57] H. Zhou, Z. Ren, D. Li, C. Xu, X. Mu, C. Lee, *Nat. Commun.* **2023**, *14*, 7316.
[58] A. John-Herpin, D. Kavungal, L. Mcke, H. Altug, *Adv. Mater.* **2021**, *33*, 2006054.